Effects on the long-wavelength geoid anomaly of lateral viscosity variations caused by stiff subducting slabs, weak plate margins and lower mantle rheology

Masaki Yoshida [a,*] Tomoeki Nakakuki [b]

[a] *Institute for Research on Earth Evolution (IFREE), Japan Agency for Marine-Earth Science and Technology (JAMSTEC), 2-15 Natsushima-cho, Yokosuka 237-0061, Japan.*

[b] *Department of Earth and Planetary Systems Science, Graduate School of Science, Hiroshima University, 1-3-1 Kagamiyama, Higashi-Hiroshima 739-8526, Japan*

Preprint submitted to Elsevier *8 August 2008*

Abstract

Instantaneous flow numerical calculations in a three-dimensional spherical shell are employed to investigate the effects of lateral viscosity variations (LVVs) in the lithosphere and mantle on the long-wavelength geoid anomaly. The density anomaly model employed is a combination of seismic tomography and subducting slab models based on seismicity. The global strain-rate model is used to represent weak (low-viscosity) plate margins in the lithosphere. LVVs in the mantle are represented on the basis of the relation between seismic velocity and temperature (i.e., temperature-dependent rheology). When highly viscous slabs in the upper mantle are considered, the observed positive geoid anomaly over subduction zones can be accounted for only when the viscosity contrast between the reference upper mantle and the lower mantle is approximately 10^3 or lower, and weak plate margins are imposed on the lithosphere. LVVs in the lower mantle exert a large influence on the geoid pattern. The calculated geoid anomalies over subduction zones exhibit generally positive patterns with quite high amplitudes compared with observations, even when the low activation enthalpy of perovskite in the lower mantle is employed. Inferred weak slabs in the lower mantle may be explained in terms of recent mineral physics results, highlighting the possibility of grain-size reduction due to the postspinel phase transition.

Key words: mantle convection, numerical calculation, subducting slab, plate margin, viscosity, geoid anomaly

* Corresponding author.
Email addresses: myoshida@jamstec.go.jp (Masaki Yoshida),
nakakuki@hiroshima-u.ac.jp (Tomoeki Nakakuki).

1 Introduction

The geoid anomaly observed on the Earth's surface (Figure 1a) reflects density anomalies and rheological structure in the present-day mantle. The longest-wavelength geoid with spherical harmonic degrees of 2 and 3 reveals that positive geoid amplitude peaks exist on the Africa-Atlantic regions, beneath which there are no known subducting plates, and the westernmost part of the Pacific plate, where the Australian and Pacific plates are subducting (Figure 1b). Consequently, it is likely that the locations of the peak positive anomaly are not related to either (1) contemporary plate-tectonic mechanisms and associated mantle downwellings (i.e., subduction zones) or (2) mantle upwellings inferred from hotspot distributions at the surface (Figure 1b) and low seismic velocity regions in the lower mantle (Figure 1d). In contrast, when the longest-wavelength components are subtracted from the observed geoid anomaly, broad positive geoid highs appear over entire subduction zones, especially the circum-Pacific trench belt (Figure 1c). This implies that the shorter-wavelength geoid anomaly may be strongly affected by plate tectonic processes and the locations of subducting plates.

Using an *a priori* numerical model of density anomalies and viscosity structure in the Earth's mantle as input to fluid dynamical models of mantle flow (i.e., the instantaneous flow model), we can calculate geoid anomalies and compare them with observations (Hager, 1984). However, analytical methods using propagator matrices are restricted to radially symmetric viscosity structures, because of mathematical complexities arising from mode coupling associated with laterally variable viscosity (e.g., Richards and Hager, 1989; Hager and Clayton, 1989).

On the other hand, plate tectonic processes induce distinct lateral viscosity variations (LVVs) in the mantle and lithosphere. Seismic tomography models illustrate that almost all subducting slabs reach the 660 km phase boundary, and that some of them penetrate into the lower mantle (Dziewonski, 1984; Tanimoto and Anderson, 1990; Fukao et al., 1992; van der Hilst et al., 1997). This indicates that the existence of LVVs may be due to "stiff" (high-viscosity) subducting plates. At the same time, plate margins, including "diffuse plate boundaries" (Gordon, 2000), induce LVVs in the lithosphere. The effective viscosity of diffuse oceanic/continental boundaries is at least one order of magnitude smaller than that of the stable plate interior (Gordon, 2000). Such a "weak" (low-viscosity) plate margin may have the potential to affect the degree of mechanical coupling between the lithosphere and subducting slabs sinking into the mantle. These two factors of LVVs need to be considered in numerical models.

Using a numerical modeling technique, we can address models incorporating LVVs and plate configuration in three-dimensional (3-D) spherical shell geometry. Plate rheology variations, arising due to stiff plate interiors and weak plate boundaries, significantly affect the long-wavelength geoid anomalies (Zhong and Davies, 1999; Yoshida et al., 2001). Zhong and Davies (1999) have shown that coupling between stiff subducting plates and weak slabs can explain the observed geoid anomaly better than stiff slabs alone. In these calculations, a subduction history model (Ricard et al., 1993; Lithgow-Bertelloni and Richards, 1998) is used to construct the density anomaly model. However, such subduction history models may lead to discrepancies with the actual slab distributions and morphologies observed in seismic tomography models. In particular, subducting slab geometries in the upper mantle inferred from subduction history modeling are somewhat broader horizontally than the geophysically observed horizontal scales of slabs.

Moresi and Gurnis (1996) has undertaken regional instantaneous flow modeling of geoid anomalies in a 3-D Cartesian geometry, and suggested that the geoid is very sensitive to lateral strength variations of subducted slabs. They concluded that, a low slab viscosity in the lower mantle comparable to that of the surround mantle is required to account for the observed geoid high over the subduction zone. Our previous work (Yoshida, 2004) has shown, on the basis of a 2-D Cartesian mantle convection model with self-consistent subducting plates, that the long-wavelength geoid anomaly is significantly affected by LVVs in the mantle: that is, by stiff subducting slabs and weak plate margins. However, the effects of such LVVs in 3-D spherical shell geometries are not yet clear. Therefore it is important to examine which mechanism is more important in determining long-wavelength geoid anomaly patterns.

In this paper, we have examined the possible effects of LVVs on the long-wavelength (spherical harmonic degree $\ell \leq 12$) geoid stemming from stiff subducting slabs, weak plate margins and lower mantle rheology, using the instantaneous flow model in a 3-D spherical shell domain. The density anomaly model used in this study has been obtained from two advanced geodynamic models; a high-resolution tomographic model and a subducting slab model based on seismicity. The global strain-rate model is used to constrain the LVV in the lithosphere, [while the LVV in the lower mantle is inferred using a plausible relation between seismic velocity and temperature (i.e., temperature-dependent viscosity).

2 Model Description

2.1 Numerical Methods

Instantaneous mantle flow in a 3-D spherical shell of 2871 km thickness is computed numerically under the Boussinesq approximation. The non-dimensionalized equations governing the instantaneous mantle flow with spatially variable viscosity are the conservation equations of mass and momentum;

$$\boldsymbol{\nabla} \cdot \boldsymbol{v} = 0, \tag{1}$$

$$-\boldsymbol{\nabla} p + \boldsymbol{\nabla} \cdot \left\{ \eta \left(\boldsymbol{\nabla} \boldsymbol{v} + \boldsymbol{\nabla} \boldsymbol{v}^{tr} \right) \right\} + Ra_i \zeta^3 \delta\rho \boldsymbol{e}_r = 0, \tag{2}$$

where $\boldsymbol{\nabla}$ is the differential operator in spherical polar coordinates (r, θ, ϕ), $\boldsymbol{v}$ the velocity vector, p the dynamic pressure, η the viscosity, $\delta\rho$ the density anomaly, $\boldsymbol{e}_r$ the unit vector in the r-direction, and the superscript tr indicates the tensor transpose. The "instantaneous Rayleigh number" Ra_i (Yoshida, 2008a) is given by,

$$Ra_i \equiv \frac{\rho_0 g b^3}{\kappa_0 \eta_0}, \tag{3}$$

where ρ_0 is the reference density, g the gravitational acceleration, $b = r_e - r_c$ the thickness of the mantle layer, κ_0 the reference thermal diffusivity, η_0 the reference viscosity, r_e the Earth's radius, and r_c the core radius. The constant ζ is defined by $\zeta \equiv r_e/b$, and the physical values used in this study are listed in Table 1. Impermeable and shear stress-free conditions are adopted at both the top (0 km-depth) and bottom (2871 km-depth) surface boundaries.

The calculations are performed using the "ConvGS" mantle convection code (e.g., Yoshida, 2008a,b), which has been benchmarked extensively (see Appendix A for details) and can handle orders of magnitude variations in viscosity. For this study, we compute the instantaneous flow field without solving the heat transport equation with time evolution. The SIMPLER algorithm is used to solve for the velocity and pressure fields from Equations 1 and 2. The calculation points of the velocity and pressure fields are arranged on a staggered grid, and a multi-color relaxation method is used to solve for the flow field. The size of the computational grid is $80(r) \times 128(\theta) \times 256(\phi) \times 2$ (two component grids; see Appendix A). The grid intervals in the radial direction is approximately 20 km (40 km) above (below) the 319 km depth. The resolution of this grid is even finer than that of the two input density models (i.e., the seismic tomography and subducting slab models, see Section 2.2), whose vertical resolutions are approximately 50 km (subducting slab model) and 150 km (seismic tomography model) and whose horizontal resolutions are both about 1300 km.

The geoid anomaly calculation itself is described in a series of papers by Hager (e.g., Hager and Richards, 1989) and our previous paper (Yoshida et al., 2001). We obtain a spherical harmonic expansion (degree ℓ and order m) of the geoid anomaly $\delta N^{\ell m}$, caused by density anomalies within the mantle interior and topographic deformation at the top and bottom surfaces:

$$\delta N^{\ell m} = \sum_{\ell=2}^{\ell_{\max}} \sum_{m=0}^{\ell} \left\{ \frac{4\pi G}{g(2l+1)} \left[\int_{r_c}^{r_e} \delta\rho^{\ell m}(r) r \left(\frac{r}{r_e}\right)^{\ell+1} dr \right.\right. \\ \left.\left. + \Delta\rho_{\mathrm{top}} \delta h_{\mathrm{top}}^{\ell m} r_e + \Delta\rho_{\mathrm{bot}} \delta h_{\mathrm{bot}}^{\ell m} r_c \left(\frac{r_c}{r_e}\right)^{\ell+1} \right] \right\}, \tag{4}$$

where G is the gravitational constant, and $\Delta\rho_{\mathrm{top}}$ and $\Delta\rho_{\mathrm{bot}}$ are the density contrasts at the top and bottom surfaces, respectively. Dynamic topography at the top and bottom surfaces is estimated as $\delta h^{\ell m}_{\rm top} = -\sigma^{rr}_{\rm top}/(\Delta\rho_{\rm top} g)$ and $\delta h^{\ell m}_{\rm bot} = \sigma^{rr}_{\rm bot}/(\Delta\rho_{\rm bot} g)$, respectively, where σ^{rr} is the normal stress acting on each boundary. Note that this equation is dimensional. In this study, $\ell_{\max} = 12$. From the definition of the geopotential field, the forbidden terms (i.e., C^0_1, C^1_1, S^1_1, C^1_2 and S^1_2, where C^m_ℓ and S^m_ℓ are sine and cosine terms of $\delta N^{\ell m}$, respectively), are subtracted from the solution.

In order to obtain the instantaneous flow field (velocity and pressure fields) of the mantle governed by Equations (1) and (2), we require models of both density anomalies ($\delta\rho(r,\theta,\phi)$) and viscosity ($\eta(r,\theta,\phi)$) throughout the mantle. In the following subsections (2.2 and 2.3), we will describe the two models used in our calculations.

2.2 Input density anomaly model

Instantaneous flow in the entire mantle is assumed to be driven by internal buoyancy sources. Shown in Figure 2a is the density anomaly model used in this study. In order to construct more realistic global density models compared with those employed in our previous work (Yoshida et al., 2001), and following our previous work of Yoshida (2004, 2008a), we have used a coupled model incorporating a global slab configuration model and a global tomography model

To model density anomalies in the lower mantle beneath the 660 km transition zone, we use the "SMEAN" tomography model (Becker and Boschi, 2002), which is a weighted average of three separate S-wave velocity models; "ngrand" (an updated version of "grand" (Grand et al., 1997)), "s20rts" (Ritsema and van Heijst, 2000) and "sb4l18" (Masters et al., 1999). The SMEAN model is expanded by spherical harmonics to $\ell = 31$ at each of 20 depths with uniform intervals throughout the mantle (see Becker and Boschi (2002) for details). We estimate density anomalies in the lower mantle from the deviation of the SMEAN model from PREM (Dziewonski and Anderson, 1981). A scaling factor used to convert velocity anomalies to density anomalies, $R_{\rho/S} \equiv \delta(\log \rho)/\delta(\log v_S)$, is expressed by the depth profile shown in Figure 2b based on result from mineral physics that take into account both anharmonic and anelastic effects (Karato, 1993).

Because even recent high-resolution global tomography models do not contain well-resolved subducting slabs, and near-surface tomography includes isostatically compensated compositional differences, i.e., continental tectosphere (e.g., Jordan, 1975), and low-velocity regions around under the mid-ocean ridges, we do not impose upper mantle density anomalies above the 660 km boundary from the SMEAN model. Instead, here we adopt a modified "regionalized upper mantle (RUM)" seismic model (Gudmundsson and Sambridge, 1998), which is based on seismicity in the upper mantle. We use the slab model expanded by spherical harmonics to $\ell = 31$. In the 410–660 km transition zone the distribution of slabs at 410 km are radially extended to the 660 km-depth because of the possible existence of aseismic slabs. For simplicity, we assume that the density anomaly of the slab is a spatially constant value, $+32\,\mathrm{kg/m^3}$, based on previous numerical models (e.g., Hager and Richards, 1989; Billen and Gurnis, 2003). As we focus here on the effects of high-density, high-viscosity subducting slabs on the geoid anomaly and try to directly compare computational results with the observed longest-wavelength-removed geoid anomaly (Figure 1c), we do not impose low-density anomaly regions in the upper mantle. Rather, in the upper mantle $\delta\rho(r, \theta, \phi)$ is zero except where there are subducting slabs (see "209 km" and "418 km" in Figure 2a).

2.3 Input viscosity model

We make viscosity models exhibiting both vertical and lateral variations. The radial viscosity variation is layered so as to define the lithosphere (0–100 km depth), asthenosphere (100–200 km), reference upper mantle (200–410 km), transition zone (410–660 km), lower mantle (660–2600 km), and bottom boundary layer (2600–2871 km) (Figure 3a). (Hereafter, we refer to the reference upper mantle layer as "the upper mantle" for simplicity.) The viscosity of the reference upper mantle is fixed at 10^{21} Pa·s (Haskell, 1935) (although dynamic topography and the geoid anomaly do not depend on the absolute viscosity of each layer itself). The viscosity contrast between the lower mantle and the upper mantle ($\Delta\eta_{\mathrm{lwm}} \equiv \eta_{\mathrm{lwm}}/\eta_{\mathrm{upm}}$) is treated as a free parameter in this study (see Section 3), where η_{lwm} and η_{upm} are the lower mantle and upper mantle viscosities, respectively. The viscosity contrast of the lithosphere relative to the upper mantle ($\Delta\eta_{\mathrm{lit}}$) is taken to be 10^4, which is in the range of the reported effective viscosity of the lithosphere (Gordon, 2000). The viscosity contrast of the asthenosphere relative to the upper mantle ($\Delta\eta_{\mathrm{ast}}$) is fixed at 10^{-1} (e.g., Bills and May, 1987; Okuno and Nakada, 1998). The viscosity contrasts of the transition zone and the bottom boundary layer relative to the upper mantle are determined by the lower mantle viscosity, and taken to be the square root of $\Delta\eta_{\mathrm{lwm}}$.

We consider LVVs caused by stiff subducting slabs or weak plate margins, or both. The viscosity contrast of the subducting slab relative to the upper mantle ($\Delta\eta_{\mathrm{slab}}$) is assumed to be spatially constant between depths of 100 and 660 km, and is taken as a characteristic parameter in this study (see Table 2 and Section 3.2 for details). Lateral viscosity variations in the lower mantle are determined by taking the temperature-dependent rheology into account, in a similar manner to that adopted for the mantle convection calculations (see Table 2 and Section 3.3 for details).

Figure 3b is a map of the viscosity distribution in the lithosphere. The viscosity of the plate margins is determined using the "Global Strain Rate Map (GSRM)" model based on geodetic and geologic observations (Kreemer et al., 2000, 2003). Diffuse plate boundaries in the lithosphere (Gordon, 2000) are also included in this model. The horizontal viscosity variation at plate margins η_{margin} is represented by

$$\eta_{\mathrm{margin}}(\theta, \phi) = \frac{\tau_{\mathrm{margin}}}{\dot{\epsilon}(\theta, \phi)}, \tag{5}$$

where $\dot{\epsilon}$ is the second invariant of the strain-rate tensor given by the GSRM model, and τ_{margin} is the second invariant of the deviatoric stress tensor, which controls the degree of viscosity variation within the plate margin. We set $\tau_{\mathrm{margin}} = 3\,\mathrm{MPa}$, which is comparable the stress drop of shallow earthquakes (Kanamori and Anderson, 1975), and is supported by numerical simulation of subduction initiation (Toth and Gurnis, 1998). The resulting averaged viscosity of the plate margin outside diffuse plate boundary regions is almost the same as that of the upper mantle. The configuration and viscosity of the plate margins are the same at all depths (0–100 km depth) in the lithosphere.

3 Results

3.1 Laterally uniform viscosity model

The scenarios investigated in this study are summarized in Table 2. We first calculated the geoid anomaly using the laterally uniform viscosity model, neglecting stiff subducting slabs, weak plate margins and the lower mantle rheology (Series 1). We then varied the viscosity contrast between the upper mantle and the lower mantle ($\Delta\eta_{\rm lwm}$) from 10 to 10^4. Shown in Figure 4 is the calculated geoid anomaly with the maximum degree of up to 12. This result shows that the geoid anomaly over the subduction zones becomes gradually positive with increasing $\Delta\eta_{\rm lwm}$. This trend is consistent with that observed in earlier pioneering work (e.g. Hager and Richards, 1989) using analytical methods, in spite of the differences between the density anomaly models used in the calculations. We have confirmed that the observed geoid highs over subduction zones arise only when $\Delta\eta_{\rm lwm}$ is approximately 10^3 (Figure 4c). When $\Delta\eta_{\rm lwm}$ is 10^4, the maximum amplitude of the geoid highs is much larger (>200 m; Figure 4d).

3.2 Effects of stiff subducting slabs and weak plate margins

In Series 2, we imposed stiff (high-viscosity) subducting slabs in the upper mantle alone on the laterally uniform viscosity model. The viscosity contrast between the subducting slabs and the upper mantle ($\Delta\eta_{\rm slab}$) is here taken to be spatially constant and the same as that of the lithosphere, i.e., $\Delta\eta_{\rm slab} = 10^4$. As in Series 1, we next varied $\Delta\eta_{\rm lwm}$ from 10 to 10^4. As shown in Figure 5a, the geoid anomaly shows strongly negative "eyes" over the Java trench and the South America trench, when $\Delta\eta_{\rm lwm}$ is 10^3 or lower. This is because surface deformations in those regions are strongly depressed due to mechanically strong coupling between the lithosphere and the stiff subducting slabs. In both these regions, the subducting slabs penetrate into the middle of mantle (e.g. Fukao et al., 2001). As deduced from the results of Series 1, when $\Delta\eta_{\rm lwm} = 10^4$ the geoid anomaly still remains quite large ($> 200\,{\rm m}$) over subduction zones.

We considered further the effects of weak (low-viscosity) plate margins in the lithosphere. Previous studies have shown that low-viscosity plate boundaries of constant width and viscosity weaken the mechanical coupling between the slab and the surface (Zhong and Davies, 1999; Yoshida et al., 2001). In Series 3, based on the GSRM model (Figure 3b), we imposed weak plate margins with horizontal viscosity variations in the lithosphere on the models of Series 2. As described in Section 2.3, the viscosity of the plate margins is determined by Equation 5. Figure 5b shows the results for Series 3. When $\Delta\eta_{\rm lwm}$ is 10^3, the positive anomaly with a maximum amplitude of approximately $100\,{\rm m}$ is reproduced over the Java and South America trenches ("A" and "B" in the right-hand map of Figure 5b). On the other hand, the amplitude of the positive geoid pattern around the Japan trench is reduced. As a result, the geoid pattern is well fit to the observation after subtracting degrees 2 and 3 (Figure 1c).

We have also examined the effects of the stiffness of the subducting slabs on the geoid by varying $\Delta\eta_{\rm slab}$. The weak plate margins are not incorporated in this case (Series 4). Compared with the results for Series 2 shown in Figure 5a, Figure 5c illustrates that the geoid anomaly over the Java and South America trenches are made positive by lowering $\Delta\eta_{\rm slab}$ ("C" and "D" in the right-hand map of Figure 5c). This is because the low-viscosity of the slab may somewhat weaken the mechanical coupling between it and the surface.

Figure 5d shows the results for Series 5, in which weak plate margins are imposed the Series 4 models shown in Figure 5c. While the geoid anomaly above subduction zones remains negative when $\Delta\eta_{\mathrm{lwm}}$ is 10^2 or lower, the positive geoid anomaly is reproduced over the Java trench when $\Delta\eta_{\mathrm{lwm}} = 10^3$ ("D" in the right-hand map of Figure 5d), and the resulting geoid anomaly again fits the observations after subtracting the longest-wavelength components.

Irrespective of the strength of the upper mantle slab, when $\Delta\eta_{\mathrm{lwm}} = 10^3$ the maximum amplitude of the positive anomaly is indeed greater than 100 m (Figures 5b and 5d), or somewhat larger than observed geoid peaks of ~ 40 m (Figure 1c). Slightly lower $\Delta\eta_{\mathrm{lwm}}$ values of 10^3 may reduce the calculated geoid peaks.

3.3 Effects of LVVs in the lower mantle

Finally, we consider the effects of LVVs in the lower mantle (660–2871 km), assuming that the viscosity of the lower mantle materials depends only on temperature via the non-dimensional Arrhenius expression

$$\eta(T) \equiv \eta_{\mathrm{ref\_lwm}} \exp\left[\frac{H_a}{T + T_{\mathrm{ref}}} - \frac{H_a}{2T_{\mathrm{ref}}}\right], \tag{6}$$

where $\eta_{\mathrm{ref\_lwm}}$ is the reference viscosity at reference temperature T_{ref}, which is fixed at 0.5. We take the non-dimensional activation parameter H_a to be $\ln 10^{10}$ (~ 23.0) based on a typical activation enthalpy value for $MgSiO_3$ perovskite of 400–500 kJ/mol, as suggested by recent mineralogical results (Yamazaki and Karato, 2001). This value is substantially lower than typical values for olivine (Karato and Wu, 1993). The temperature T is determined from the seismic velocity anomaly:

$$\delta(\log v_S) = \frac{\partial(\log v_S)}{\partial T}\delta T \equiv A_{v_S T}\delta T, \tag{7}$$

where $A_{v_S T}$ is the temperature derivative of S-wave velocities in the mantle, and given by the depth profile shown in Figure 2c based on mineral physics results (e.g. Karato, 1993). Following Gurnis et al. (2000), we treat the non-dimensional form of the temperature as follows;

$$T \equiv T_{\mathrm{ref}} + \frac{1}{A_{v_S T}\Delta T}\delta(\log v_S), \tag{8}$$

where ΔT is the temperature difference across the mantle, 2500 K. As in Series 1–5, the viscosity contrast of the lower mantle relative to the upper mantle is defined by $\Delta\eta_{\mathrm{lwm}} \equiv \eta_{\mathrm{ref\_lwm}}/\eta_{\mathrm{upm}}$, and is varied from 10 to 10^4. In order to stabilize the numerical calculations, we constrain the viscosity $\eta(T)$ in Equation (6) to between $\Delta\eta_{\mathrm{ast}}$ $(= 10^{-1})$ and $\Delta\eta_{\mathrm{slab}}$ $(\leq 10^4)$. Note that the viscosity distribution in the bottom boundary layer (2600–2871 km depth) is replaced by that determined by Equation (6) in this scenario.

Shown in Figure 6 are the results for Series 6. We observe that, in comparison with Series 3 (Figure 5b) which does not have LVVs in the lower mantle, the Series 6 geoid anomaly over subduction zones exhibits generally positive patterns with quite high amplitudes of up to $\sim$150–200 m with respect to observations, when $\Delta\eta_{\mathrm{lwm}} = 10^3$. This is because the negative buoyancy of the subducting slab is supported by highly viscous, cold materials in the deep mantle. The bottom part of a subducting slab is subject to a resistance force at depth and is sufficiently stiff to transmit the stress back to the top boundary. This weakens the slab pull force on the surface lithosphere so that the topographic depression at the subduction zone is reduced. When H_a is increased to $\ln 10^{50}$ (~ 115.1) using the olivine activation values, the maximum amplitude of the calculated geoid is much higher (~ 250–$300\,\mathrm{m}$) than that observed.

4 Discussion

The advantage of using an instantaneous flow model is that we can constrain the rheological (viscosity) structure of the present-day (or nearly present-day) mantle, by assuming the density anomaly models *a priori*. In this study, by implementing a numerical calculation technique, we can address models incorporating lateral variations in viscosity. The input density anomaly model is determined from the depth profile of $R_{\rho/s}$, which is obtained from independent studies, i.e., mineral physics. The value of $R_{\rho/s}$ at each depth depends on the degree of chemical heterogeneity in the mantle. While most of the velocity anomalies in the mantle can be ascribed to temperature anomalies, the lowermost mantle is difficult to explain in terms of temperature effects alone (e.g., Karato, 2003). However our previous experiments without LVVs showed that whether there are low density regions in the lower mantle or not hardly affects the surface signatures of either the geoid anomaly or topography (Yoshida, 2004). This conclusion is unchanged by the incorporation of LVVs.

One of the key findings of this study is that the calculated geoid anomaly is sensitive to the existence of weak plate margins in the lithosphere. When weak plate margins are imposed, the geoid anomaly over subduction zones tends to be good fit to observations, irrespective of the strength of the upper mantle slabs (Series 3 and 5 in Figures 5b and 5d). Because weak plate margins relax the mechanical coupling between the slab and the surface, the negative anomaly over the Java and the South America trenches is reduced. As a result, when $\Delta\eta_{\mathrm{lwm}}$ is approximately 10^3, the amplitude of the geoid high is comparable to observations over the subduction zones. This feature has not been highlighted in previous studies.

In order to accurately represent the observed positive geoid anomaly over subduction zones, we must take the viscosity contrast between the upper mantle and the lower mantle ($\Delta\eta_{\mathrm{lwm}}$) to be approximately 10^3 (or lower), if lower mantle LVVs are neglected. This optimum $\Delta\eta_{\mathrm{lwm}}$ value is one or two orders of magnitude larger than the corresponding value determined by the classical analysis of the geoid anomaly over subduction zones, $\Delta\eta_{\mathrm{lwm}} = 30$, which incorporated a density anomaly model based on seismicity (Hager, 1984). That value has been reinforced by the results of numerical modeling of mantle convection (Gurnis and Hager, 1988) and post-glacial rebound analysis (e.g. Peltier, 1998; Lambeck and Johnston, 1998).

However more recent research favors models with larger $\Delta\eta_{\mathrm{lwm}}$ values. Hager and Richards (1989) showed that the optimum $\Delta\eta_{\mathrm{lwm}}$ value is 300 when a seismic tomography model is used for the density anomaly model. Likewise, numerical results based on subduction history modeling by Zhong and Davies (1999) yielded an optimum value for $\Delta\eta_{\mathrm{lwm}}$ of 600 assuming $\Delta\eta_{\mathrm{lit}} = 300$, that the slab viscosity is the same as the surrounding mantle, and that weak plate margins are present. That model is comparable with the Series 1 scenario in our study and the results are close to our preferred $\Delta\eta_{\mathrm{lwm}}$ value. Furthermore, recent results from the joint inversion of mantle convection and glacial isostatic adjustment data have implied an increase in mid-lower mantle viscosity by a factor of around 1000 with respect to the upper mantle viscosity (Mitrovica and Forte, 2004). Forte and Mitrovica (2001) have suggested based on the joint inversion of seismic tomography data and various geodynamic data, that the high-viscosity layer near 2000 km depth strongly suppresses convective mixing in the deep mantle. Clearly, the viscosity contrast between the upper (or shallow) and the lower (or deep) mantle remains a controversial topic.

Lateral viscosity variations in the lower mantle may provide a candidate mechanism for reducing our optimum $\Delta\eta_{\mathrm{lwm}}$ value. We have investigated the effects of stiff slabs in the lower mantle by taking temperature-dependent viscosity into account. Our results imply that stiff slabs in the lower mantle tend to produce a poor fit to the observed geoid (Series 6 in Figure 6). The large effects of stiff subducting slabs on the long-wavelength geoid anomaly have already been reported by Zhong and Davies (1999). They showed that the geoid pattern changes substantially, even when the viscosity contrast between the subducting slab and the ambient mantle at the same depth is only 10. Zhong and Davies (1999) emphasized that a deep slab (2000 km-deep to CMB) disconnected from the surface (e.g., over the North Pacific region) generates a strong positive anomaly if the slab has high-viscosity, and therefore that "isolated" slabs in the lower-most mantle may be weaker than the surrounding mantle. In contrast, using our model incorporating seismic tomography results in the lower mantle, the geoid anomaly over the North Pacific region is found to be relatively low ("A" in Figure 6c), which seems to be inconsistent with observations (Figure 1c). The difference between the earlier study of Zhong and Davies (1999) and ours arises from discrepancies in the distribution and morphology of the high-density region in the lower mantle. However, with the exception of this discrepancy, we can be sure that LVVs in the lower mantle exert a large influence on the geoid pattern.

Considering now the effects of the lower mantle's rheology, we see that the geoid anomaly over subduction zones exhibits generally positive patterns of quite high amplitude with respect to observations, even when the low activation enthalpy of perovskite is used for the lower mantle. Our results imply that lower mantle slabs lose their high-viscosity characteristics at 660 km depth. Some mineralogical studies have raised the possibility of weaker slabs in the lower mantle, in light of grain size reduction due to mineralogical transformations in upper mantle rock. The viscosity of the slab in the lower mantle may be reduced by grain size reduction as a result of the ringwoodite to perovskite-magnesiowüstite phase transition (Ito and Sato, 1991; Kubo et al., 2000).

Seismic tomography models show that subducting slabs are deformed and stagnated in some of the phase transition zones (Fukao et al., 1992; van der Hilst et al., 1997; Fukao et al., 2001; Zhao, 2004). Such stagnant slabs may introduce notable viscosity variations in the phase transition zone and may thereby affect the geoid anomaly at the scale of wavelengths less than a few thousand kilometers. Further work is needed to address the effects of the configuration and rheology of stagnant slabs on the geoid pattern using higher-resolution global tomography models more clearly showing the configuration of subducting plates (e.g., Li et al., 2008). Also the emergence of higher-resolution tomography images of the upper mantle will be help to improve the density anomaly model in which we now assumed that $\delta\rho$=0 except slab regions. The imposed upper-mantle density anomaly may explain broadly positive geoid anomalies on the Africa-Atlantic regions and the westernmost part of the Pacific plate, and then reproduce the "total" geoid anomaly including longest-wavelength components (Figure 1a). In particular, low-density anomaly regions of the upper mantle may exert a large influence on the long-wavelength geoid anomaly and dynamic topography. For instance, using a regional seismic tomography model with the highly-resolved mantle beneath the French Polynesia region, Adam et al. (2007) have shown that observed dynamic topography is well reproduced through an instantaneous flow model.

In spite of the uncertainties associated with modeling density and viscosity fields in the mantle, we believe that our results form a starting point for further studies of more sophisticated models at regional or global scales. For example, the effects on the geoid anomaly of LVVs arising from compositional variations of mantle materials (e.g., Becker et al., 1999; Samuel and Farnetani, 2005) should be addressed in the future, in conjunction with geochemical and mineral physics experiments.

5 Conclusions

We have examined the possible effects of lateral viscosity variations on the long-wavelength ($\ell \leq 12$) geoid anomaly by using instantaneous flow calculations in a 3-D spherical shell model. The density model used in this study is constructed by combining a high-resolution tomography model with a subducting slab model based on seismicity. A global strain-rate model has been used to describe LVVs in the lithosphere, and LVVs in the lower mantle have been represented in terms of the relation between seismic velocity and temperature (i.e., the temperature-dependent viscosity). Using these new geodynamic models, we have drawn the following conclusions, which may provide new constraints on the viscosity structure of the mantle.

(1) In the laterally uniform viscosity model, the observed positive geoid highs over subduction zones arise only when the viscosity contrast between the reference upper mantle and the lower mantle is approximately 10^3 or lower.

(2) Considering highly viscous slabs in the upper mantle, the geoid patterns under the Java and South American trenches are depressed and exhibit negative anomalies. However when weak plate margins are imposed, the calculated geoid anomaly over the subduction zones yields a good fit to observations, irrespective of the strength of the upper mantle slabs.

(3) Lateral viscosity variations in the lower mantle exert a large influence on the geoid pattern. However the geoid anomaly over subduction zones shows a generally positive pattern of quite high amplitude compared with observations, even when the low activation enthalpy of perovskite in the lower mantle is considered. The existence of weak slabs in the lower mantle is substantiated by recent mineral physics results.

Acknowledgments

The authors are grateful to Craig O'Neill and Justin Freeman for their careful reviews. Calculations were carried out on super-computers facilities (SGI Altix 4700) of the Japan Agency for Marine-Earth Science and Technology. Most of the figures were produced using the Generic Mapping Tools (GMT) released by Wessel and Smith (1998). M.Y. was supported by the "Stagnant Slab Project", the Grant-in-Aid for Scientific Research on Priority Areas (No. 16075205) and for Young Scientists (B) (No. 20740260) from the Ministry of Education, Culture, Sports, Science and Technology, Japan.

References

Adam, C., Yoshida, M., Isse, T., Suetsugu, D., Shiobara, H., Kanazawa, T., Fukao, Y., Barruol, G., 2007. French Polynesia hotspot swells explained by dynamic topography. Eos Trans. AGU Fall Meet. Suppl. 88 (52), T21B–0599.

Becker, T. W., Boschi, L., 2002. A comparison of tomographic and geodynamic mantle models. Geochem. Geophys. Geosyst. 3, 382–394, 10.1029/2001GC000168.

Becker, W., Kellogg, J. B., O'Connell, R. J., 1999. Thermal constraints on the survival of primitive blobs in the lower mantle. Earth Planet. Sci. Lett 171, 351–365.

Bercovici, D., Schubert, G., Glatzmaier, G. A., Zebib, A., 1989. Three dimensional thermal convection in a spherical shell. J. Fluid Mech. 206, 75–104.

Billen, M. I., Gurnis, M., 2003. Comparison of dynamic flow models for the Central Aleutian and Tonga-Kermadec subduction zones. Geochem. Geophys. Geosyst. 4 (4), 1035, 10.1029/2001GC000295.

Bills, B. G., May, G. M., 1987. Lake Bonneville: constraints on lithospheric thickness and upper mantle viscosity from isostatic warping of Bonneville, Provo, and Gilbert Stage shorelines. J. Geophys. Res. 92, 11493–11508.

Davies, G. F., 1988. Ocean bathymetry and mantle convection: 1. large-scale flow and hotspots. J. Geophys. Res. 93, 10467–10480.

Davies, G. F., 1992. Temporal variation of the Hawaiian plume flux. Earth Planet. Sci. Lett. 113, 277–286.

Dziewonski, A. M., 1984. Mapping the lower mantle: Determination of lateral heterogeneity in P velocity up to degree and order 6. J. Geophys. Res. 89, 5929–5952.

Dziewonski, A. M., Anderson, D. L., 1981. Preliminary reference Earth model. Phys. Earth Planet. Inter. 25, 297–356.

Forte, A. M., Mitrovica, J. X., 2001. Deep-mantle high-viscosity flow and thermochemical structure inferred from seismic and geodynamic data. Nature 410, 1049–1056.

Fukao, Y., Obayashi, M., Inoue, H., Nenbai, M., 1992. Subducting slabs stagnant in the mantle transition zone. J. Geophys. Res. 97 (B4), 4809–4822.

Fukao, Y., Widiyantoro, S., Obayashi, M., 2001. Stagnant slabs in the upper and lower mantle transition region. Rev. Geophys. 39, 291–323.

Gordon, R. G., 2000. Diffuse oceanic plate boundaries: Strain rates, vertically averaged rheology, and comparisons with narrow plate boundaries and stable plate interiors. In: Richards, M. R., Gordon, G., van der Hilst, R. D. (Eds.), History and Dynamics of Global Plate Motions. Vol. 121 of Geophysical Monograph. American Geophysical Union, Washington, DC, pp. 143–159.

Grand, S. P., van der Hilst, R. D., Widiyantoro, S., 1997. Global seismic tomography; A snapshot of convection in the Earth. GSA Today 7, 1–7.

Gudmundsson, O., Sambridge, M., 1998. A regionalized upper mantle (RUM) seismic model. J. Geophys. Res. 103 (B4), 7121–7136.

Gurnis, M., Hager, B. H., 1988. Controls of the structure of subducted slabs. Nature 335, 317–321.

Gurnis, M., Mitrovica, J. X., Ritsema, J., van Heijst, H. J., 2000. Constraining mantle density structure using geological evidence of surface uplift rates: The case of the African Superplume. Geochem. Geophys. Geosyst. 1 (7), ,10.1029/1999GC000035.

Hager, B. H., 1984. Subducted slabs and the geoid: constraints on mantle rheology and flow. J. Geophys. Res. 89, 6003–6015.

Hager, B. H., Clayton, R. W., 1989. Constraints on the structure of mantle convection using seismic observations, flow models and the geoid. In: Peltier, W. R. (Ed.), Mantle Convection: Plate Tectonics and Global Dynamics. Gordon and Breach, New York, pp. 657–763.

Hager, B. H., Richards, M. A., 1989. Long-wavelength variations in Earth's geoid: physical models and dynamical implications. Philos. Trans. R. Soc. Lond. A 328, 309–327.

Haskell, N. A., 1935. The motion of a fluid under the surface load. Physics 6, 265–269.

Ito, E., Sato, H., 1991. Aseismicity in the lower mantle by superplasticity of the descending slab. Nature 351, 140–141.

Jordan, T. H., 1975. The continental tectoshere. Rev. Geophys 13, 1–12.

Kanamori, H., Anderson, D., 1975. Theoretical basis of some empirical relations inseismology. Bull. Seismol. Soc. Am. 65, 1073–1095.

Karato, S., 1993. Importance of anelasticity in the interpretation of seismic tomography. Geophys. Res. Lett. 20 (15), 1623–1626.

Karato, S., Wu, P., 1993. Rheology of the upper mantle: A synthesis. Science 260, 771–778.

Karato, S. I., 2003. The Dynamic Structure of the Deep Earth: An Interdisciplinary Approach. Princeton Univ. Press, Princeton, NJ.

Kreemer, C., Haines, J., Holt, W. E., Blewitt, G., Lavallee, D., 2000. On the determination of a global strain rate model. Earth Planet. Space 52, 765–770.

Kreemer, C., Holt, W. E., Haines, A. J., 2003. An integrated global model of present-day plate motions and plate boundary deformation. Geophys. J. Int. 154, 8–34.

Kubo, T., Ohtani, E., Kato, T., Urakawa, S., Suzuki, A., Kanbe, Y., Funakoshi, K., Utsumi, W., Fujino, K., 2000. Formation of metastable assemblages and mechanisms of the grain-size reduction in the postspinel transformation of Mg2SiO4. Geophys. Res. Lett. 27 (6), 807–810.

Lambeck, K., Johnston, P., 1998. The viscosity of the mantle: evidence from analyses of glacial rebound phenomena. In: Jackson, I. (Ed.), The Earth's Mantle: Composition, Structure, and Evolution. Cambridge University Press, Cambridge, pp. 461–502.

Lemoine, F. G., Kenyon, S. C., Factor, J. K., R. G. Trimmer, R., Palvis, N. K., Chinn, D. S., Cox, C. M., Klosko, S. M., Luthcke, S. B., Torrence, M. H., Wang, Y. M., Williamson, R. G., Palvis, E. C., Rapp, R. H., Olson, T. R., 1998. The development of the NASA GSFC and the National Imagery and Mapping Agency (NIMA) Geopotential Model EGM96. Tech. rep., NASA/TP-1998-206861.

Li, C., van der Hilst, R. D., Engdahl, E. R., Burdick, S., 2008. A new global model for P wave speed variations in Earth's mantle. Geochem. Geophys. Geosyst. 9, Q05018, doi:10.1029/2007GC001806.

Lithgow-Bertelloni, C., Richards, M. A., 1998. The dynamics of cenozoic and mesozoic plate motions. Rev. Geophys. 36, 27–78.

Masters, G., Bolton, H., Laske, G., 1999. Joint seismic tomography for p and s velocities: How pervasive are chemical anomalies in the mantle? Eos Trans. AGU Spring Meet. Suppl. 80 (17), S14.

McNamara, A. K., Zhong, S., 2005. Degree-one mantle convection: Dependence on internal heating and temperature-dependent rheology. Geophys. Res. Lett. 32, L01301, 10.1029/2004GL021082.

Mitrovica, J. X., Forte, A. M., 2004. A new inference of mantle viscosity based upon joint inversion of convection and glacial isostatic adjustment data. Earth Planet. Sci. Lett. 225, 177–189.

Moresi, L., Gurnis, M., 1996. Constraints on the lateral strength of slabs from three-dimensional dynamic flowmodels. Earth Planet. Sci. Lett. 138, 15–28.

Nakiboglu, S. M., 1982. Hydrostatic theory of the Earth and its mechanical implications. Phys. Earth Planet. Inter. 28, 302–311.

Okuno, J., Nakada, M., 1998. Rheological structure of the upper mantle inferred from the holocene sealevel change along the west coast of kyushu, japan. In: Wu, P. (Ed.), Dynamics of the Ice Age Earth: A Modern Perspective. Trans Tech Publications, Brandrain, Switzerland, pp. 443–458.

Peltier, W. R., 1998. Postglacial variations in the level of the sea: implications for climate dynamics and solid-earth geophysics. Rev. Geophys. 36, 603–689.

Ratcliff, J. T., Schubert, G., Zebib, A., 1996. Steady tetrahedral and cubic patterns of spherical shell convection with temperature-dependent viscosity. J. Geophys. Res. 101 (B11), 25,473–25,484.

Ribe, N., Christensen, U., 1999. The dynamical origin of Hawaiian volcanism. Earth Planet. Sci. Lett. 171, 517–531.

Ricard, Y., Richards, M. A., Lithgow-Bertelloni, C., Stunff, Y. L., 1993. A geodynamic model of mantle density heterogeneity. J. Geophys. Res. 98, 21895–21909.

Richards, M. A., Hager, B. H., 1989. Effects of lateral viscosity variation on long-wavelength geoid anomalies and topography. J. Geophys. Res. 94, 10299–10313.

Richards, M. A., Yang, W. S., Baumgardner, J. R., Bunge, H. P., 2001. Role of a low-viscosity zone in stabilizing plate tectonics: Implications for comparative terrestrial planetology. Geochem. Geophys. Geosyst. 2 (8), 10.1029/2000GC000115.

Ritsema, J., van Heijst, H. J., 2000. Seismic imaging of structural heterogeneity in Earth's mantle: Evidence for large-scale mantle flow. Sci. Progr. 83, 243–

259.

Samuel, H., Farnetani, C. G., 2005. Heterogeneous lowermost mantle: Compositional constraints and seismological observables. In: van der Hilst, R. D., Bass, J. D., Matas, J., Trampert, J. (Eds.), Earth's Deep Mantle. Vol. 160 of Geophysical Monograph. American Geophysical Union, Washington, DC, pp. 101–116.

Schilling, J. G., 1991. Fluxes and excess temperatures of mantle plumes inferred from their interaction with migrating mid-ocean ridges. Nature 352, 397–403.

Sleep, N. H., 1990. Hotspots and mantle plumes: some phenomenology. J. Geophys. Res. 95, 6715–6736.

Steinberger, B., 2000. Plumes in a convecting mantle: Models and observations for individual hotspots. J. Geophys. Res. 105 (B5), 11127–11152.

Stemmer, K., Harder, H., Hansen, U., 2006. A new method to simulate convection with strongly temperatureand pressure-dependent viscosity in a spherical shell: Applications to the Earth's mantle. Phys. Earth Planet. Inter. 157, 223–249.

Tanimoto, T., Anderson, D. L., 1990. Long-wavelength S-wave velocity structure throughout the mantle. Geophys. J. Int. 100, 327–336.

Toth, J., Gurnis, M., 1998. Dynamics of subduction initiation at pre-existing fault zones. J. Geophys. Res. 103, 18053–18067.

van der Hilst, R. D., Widiyantoro, S., Engdahl, E. R., 1997. Evidence for deep mantle circulation from global tomography. Nature 386, 578–584.

Wessel, P., Smith, W. H. F., 1998. New, improved version of the Generic Mapping Tools released. EOS Trans. AGU 79 (47), 579.

Yamazaki, D., Karato, S., 2001. Some mineral physics constraints on the rheology and geothermal structure of earth's lower mantle. American Mineralogist 86, 385–391.

Yoshida, M., 2004. Possible effects of lateral viscosity variations induced by plate-tectonic mechanism on geoid inferred from numerical models of mantle convection. Phys. Earth Planet. Inter. 147 (1), 67–85.

Yoshida, M., 2008a. Core-mantle boundary topography estimated from numerical simulations of instantaneous mantle flow. Geochem. Geophys. Geosyst. 9 (7), Q07002, 10.1029/2008GC002008.

Yoshida, M., 2008b. Low-degree mantle convection with different heating modes and compressibility. Geophys. Res. Lett., submitted.

Yoshida, M., Honda, S., Kido, M., Iwase, Y., 2001. Numerical simulation for the prediction of the plate motions: Effects of lateral viscosity variations in the lithosphere. Earth Planet. Space 53 (7), 709–721.

Yoshida, M., Kageyama, A., 2004. Application of the Yin-Yang grid to a thermal convection of a Boussinesq fluid with infinite Prandtl number in a three-dimensional spherical shell. Geophys. Res. Lett. 31 (12), L12609, 10.1029/2004GL019970.

Yoshida, M., Kageyama, A., 2006. Low-degree mantle convection with strongly temperature- and depth-dependent viscosity in a three-dimensional spherical shell. J. Geophys. Res. 111 (B3), B03412, 10.1029/2005JB003905.

Yoshida, M., Nakakuki, T., Kido, M., 2007. Roles of lateral viscosity variations caused by stiff subducting slabs and weak plate margins on long-wavelength geoid anomaly. In: paper presented at 24th General Assembly, Int. Union of Geod. and Geophys. JSS011-2153, Perugia, Italy, 2–13, July.

Zhao, D., 2004. Global tomographic images of mantle plumes and subducting slabs: insight into deep Earth dynamics. Phys. Earth Planet. Inter. 146, 3–34.

Zhong, S., Davies, G. F., 1999. Effects of plate and slab viscosities on the geoid. Earth Planet. Sci. Lett. 170, 487–496.

Zhong, S., Zuber, M. T., Moresi, L., Gurnis, M., 2000. Role of temperature-dependent viscosity and surface plates in spherical shell models of mantle convection. J. Geophys. Res. 105 (B5), 11,063–11,082.

Meaning of symbols	Value
Earth's radius, r_e	6371 km
Core radius, r_c	3500 km
Thickness of the mantle, b	2871 km
Gravitational constant, G	$6.67 \times 10^{-11}\,\mathrm{Nm^2/kg^2}$
Gravitational acceleration, g	$9.82\,\mathrm{m/s^2}$
Density contrast at top surface, $\Delta\rho_{\mathrm{top}}$	$2360.76\,\mathrm{kg/m^3}$
Density contrast at bottom surface, $\Delta\rho_{\mathrm{bot}}$	$4337.04\,\mathrm{kg/m^3}$
Reference density, ρ_0	$3300\,\mathrm{kg/m^3}$
Reference viscosity in the upper mantle, η_0	$10^{21}\,\mathrm{Pa{\cdot}s}$
Reference thermal diffusivity, κ_0	$10^{-6}\,\mathrm{m^2/s}$
Instantaneous Rayleigh number, Ra_i	7.67×10^8

Table 1

The physical values used in this study.

Series	$\Delta\eta_{\mathrm{slab}}$	WPM	LM-LVV	Figure
1	1	No	No	4
2	10^4	No	No	5a
3	10^4	Yes	No	5b
4	10^2	No	No	5c
5	10^2	Yes	No	5d
6	10^4	Yes	Yes	6

Table 2

Summary of the numerical models constructed in this study. $\Delta\eta_{\mathrm{slab}}$ is the viscosity contrast of the upper mantle slab relative to the reference upper mantle. Abbreviations WPM and LM-LVV denote weak (low-viscosity) plate margins and lateral viscosity variations in the lower mantle, respectively. The radial viscosity variation is layered to represent the lithosphere (0–100 km depth), asthenosphere (100–200 km), reference upper mantle (200–410 km), transition zone (410–660 km), lower mantle (660–2600 km), and bottom boundary layer (2600–2871 km). In all models, the viscosity contrast of the lower mantle relative to the upper mantle ($\Delta\eta_{\mathrm{lwm}}$) is treated as a free parameter and varied from 10 to 10^4. The viscosity contrasts of the lithosphere and the asthenosphere relative to the upper mantle are fixed at 10^4 and 10^{-1}, respectively. The viscosity contrast of the transition zone and the bottom boundary layer relative to the upper mantle are taken to be the square root of $\Delta\eta_{\mathrm{lwm}}$ (see text and Figure 3a for details).

Fig. 1. (a–c) Observed geoid anomaly at spherical harmonic degrees of (a) 2 to 360, (b) 2 and 3, (c) 4 to 12, based on the EGM96 potential model (Lemoine et al., 1998) after correction for the hydrostatic shape (Nakiboglu, 1982). The contour intervals are 20 m. In (b), the distribution of 44 hotspots is shown by purple open circles, whose sizes represent the magnitude of the buoyancy flux of each hotspot. The buoyancy flux data are taken from several papers (Davies, 1988; Sleep, 1990; Schilling, 1991; Davies, 1992; Ribe and Christensen, 1999; Steinberger, 2000). Small hotspots of unknown buoyancy flux are not shown. (d) S-wave seismic velocity anomaly (δv_s) in the lower mantle (1507 km depth) from the SMEAN model (Becker and Boschi, 2002). In (a)-(d), plate boundaries are shown for reference.

Fig. 2. (a) Density anomaly model used in this study. The seismic slab model (Gudmundsson and Sambridge, 1998) and the seismic tomography model (Becker and Boschi, 2002) are combined. (b–c) Depth profiles of (b) $R_{\rho/S} = \delta(\log \rho)/\delta(\log v_S)$ and (c) $-A_{v_S T} = -\partial(\log v_S)/\partial T$ applied to each model. See text for details.

Fig. 3. (a) Depth profile of the vertical viscosity. The viscosity contrast between the upper and the lower mantle $\Delta\eta_{\mathrm{lwm}}$ is varied between 10 (blue solid line) and 10^4 (blue dashed line). The viscosities of the transition zone and the bottom boundary layer are equal to the square root of $\Delta\eta_{\mathrm{lwm}}$. (b) Distribution of the lateral viscosity variations in the lithosphere inferred from the GSRM model (Kreemer et al., 2000, 2003). See text for details.

Fig. 4. Calculated geoid anomaly for models in Series 1. The viscosity contrasts between the upper and the lower mantle $\Delta\eta_{\mathrm{lwm}}$ are (a) 10^1, (b) 10^2, (c) 10^3, and (d) 10^4. The contour intervals are 50 m. Plate boundaries are shown for reference.

Fig. 5. Calculated geoid anomaly for models in (a) Series 2, (b) Series 3, (c) Series 4, and (d) Series 5. The viscosity contrasts between the upper mantle and lower mantle, $\Delta\eta_{\mathrm{lwm}}$, are 10^2 (left-hand map in each row) and 10^3 (right-hand map). The contour intervals are 50 m. Plate boundaries are shown for reference. See the text for explanation of symbols "A"–"D" and further details.

Fig. 6. Calculated geoid anomaly for models in Series 6. The viscosity contrasts between the upper mantle and the lower mantle, $\Delta\eta_{\mathrm{lwm}}$, is (a) 10^1, (b) 10^2, (c) 10^3, and (d) 10^4. The contour intervals are 50 m. Plate boundaries are shown for reference. See text for explanation of symbol "A" and further details.

A Benchmark calculation for ConvGS

The ConvGS (Convection in a Global Spherical-shell) used in this study is a mantle convection code developed by one of authors (M.Y.) at IFREE, JAMSTEC, and first used in the work of Yoshida et al. (2007). The finite volume method is used for the discretization of the basic equations governing mantle convection (i.e., the conservation equations of mass, momentum and energy) on staggered grid, rather than the finite difference method (Yoshida and Kageyama, 2004, 2006) and the collocated grid (e.g., Yoshida et al., 2001) implemented in our previous code. In comparison with the finite difference method, the advantage of the finite volume method is its conservation of physical values and numerical stability for convection models incorporating strongly variable viscosity. The computational grid used here for the Yin-Yang grid, which is two component longitude-latitude grids covering a spherical shell (Yoshida and Kageyama, 2004). M.Y. has also developed another code ConvRS (Convection in a Regional Spherical-shell) to solve the mantle convection problem in a regional 3-D spherical shell geometry; that code has been used in a separate study (Adam et al., 2007). ConvGS and ConvRS are applicable to mantle convection modeling with rock compressibility, non-Newtonian rheology, phase change, and other geophysical processes. In this study, the parallel calculation was performed using the one-dimensional domain-decomposition method with MPI.

Because the benchmark calculation to verify the ConvGS has not been reported in a previous paper (Yoshida, 2008a), we discuss it here. To verify the validity and numerical accuracy of ConvGS, we carried out two types of the benchmark calculation. First, following earlier studies (Richards et al., 2001;

Yoshida and Kageyama, 2004; Stemmer et al., 2006), we performed benchmark calculations for a number of mantle convection codes using spectral, finite element, finite difference method, and finite volume methods. Confirming the validity of the mantle convection calculation including the time advance is equivalent to confirming the validity of the instantaneous mantle flow model, as calculating the instantaneous mantle flow using Equations 1 and 2 is the same numerical problem as calculating the steady-state mantle convection flow field at a specific time.

The results of the benchmark calculations are summarized in Tables A. 1 and A. 2. We performed the calculation for models with low Rayleigh number ($Ra<10^5$) and constant viscosity or weakly variable viscosity due to the temperature-dependent rheology. We computed the Nusselt number and the root-mean square velocity for steady-state convections with the tetrahedral and cubic symmetric mantle convection regimes (e.g., Bercovici et al., 1989). The viscosity is given by $\eta(T) = \exp[-E(T - 0.5)]$ where T is the non-dimensional temperature and E is the non-dimensional activation energy. The size of the computational domain is $64(r) \times 32(\theta) \times 96(\phi) \times 2$ (two component grids). In spite of the differences in discretization methods, numerical techniques, and the number of grid points between the codes, the results for ConvGS agree well with each of them. In particular, when compared with another finite volume-based code incorporating the cubed-sphere grid (Stemmer et al., 2006), we observe that the differences between two codes (see "SH06" and "Yo08" in Tables A.1 and A.2) are overall within 0.5%.

Next, for unsteady, time-dependent convection models with realistic Rayleigh numbers and strongly variable viscosity, we performed calculations similar to those presented by Ratcliff et al. (1996) using the finite volume method and by McNamara and Zhong (2005) using the finite element method. We illustrate two results for models with Rayleigh numbers of 10^7; one represents a purely bottom-heated mantle with viscosity contrast across the mantle due to temperature-dependent rheology (γ_η) of 10^2 and the other represents a bottom- and internally-heated mantle with $\gamma_\eta = 10^4$. In the latter model, the non-dimensional internal heating rate scaled by the Earth's radius is taken to be 30.4. The viscosity is given by $\eta(T) = \exp[2E/(T+1) - E]$, and the size of the computational domain is $100 \times 100 \times 300 \times 2$. As shown in Figure A.1, two convection patterns reach a nearly steady-state, long-wavelength thermal heterogeneity dominated by degree-two and degree-one (i.e., the spherical harmonic degrees of 2 and 1, respectively), which are comparable to the results of Ratcliff et al. (1996) and McNamara and Zhong (2005), respectively. In other words, in spite of the numerically challenging test configurations dictated by realistic Rayleigh numbers and strong variations in viscosity, we can reproduce the convection patterns obtained by other numerical codes. We have therefore verified the numerical accuracy of our new code. We will report on models incorporating variable magnitudes of the viscosity contrast in a later paper addressing the effects of temperature-dependent rheology and different heating modes on mantle convection patterns (Yoshida, 2008b).

T/C	Ra	γ_η	Br89	Rt96	Zh00	Rc01	YK04	SH06	Yo08
T	2.0e3	1	2.2507	2.1740	2.218	-	2.2025	-	2.2045
T	7.0e3	1	3.4657	3.4423	3.519	3.4160	3.4430	3.4864	3.4911
T	1.4e4	1	-	4.2028	-	4.2250	4.2395	-	4.2764
T	7.0e3	20	-	3.1615	-	-	3.1330	3.1447	3.1505
C	7.0e3	1	-	3.5806	-	-	3.5554	3.5982	3.6114
C	7.0e3	20	-	3.3663	-	-	3.3280	3.3423	3.3531

Table A.1

Nusselt numbers obtained from various numerical codes. The model parameters are the Rayleigh number (Ra) and the viscosity contrast across the mantle (γ_η). Read "2.0e3" as 2.0×10^3. The letters "T" and "C" denote the tetrahedral ("T") and cubic ("C") symmetric mantle convection regimes, respectively (e.g., Bercovici et al., 1989). "Br89" denotes Bercovici et al. (1989) (employing the spectral method), "Rt96" Ratcliff et al. (1996) (finite volume method), "Zh00" Zhong et al. (2000) (finite element method), "Rc01" Richards et al. (2001) (finite element method), "YK04" Yoshida and Kageyama (2004) (finite difference method), "SH06" Stemmer et al. (2006) (finite volume method), and "Yo08" the ConvGS code described by Yoshida (2008a).

T/C	Ra	γ_η	Rt96	YK04	SH06	Yo08
T	2.0e3	1	12.14	12.1246	-	12.5774
T	7.0e3	1	32.19	32.0481	32.5849	32.4639
T	1.4e4	1	50.27	50.0048	-	50.1971
T	7.0e3	20	25.69	26.1064	25.7300	25.6594
C	7.0e3	1	30.87	30.5197	31.0226	30.8933
C	7.0e3	20	25.17	25.3856	24.9819	24.9154

Table A.2

Root-mean-square velocities obtained from various numerical codes. The parameters and the meaning of "T" and "C" are the same as Figure A.1.

Fig. A.1. Three-dimensional view of the mantle convection pattern for models incorporating (a) $\gamma_\eta = 10^2$ and purely bottom-heating, and (b) $\gamma_\eta = 10^4$ and bottom- and internal-heating. Isosurfaces of the non-dimensional residual temperature δT (i.e., the deviation from the horizontally averaged temperature at each depth) for models with temperature-dependent rheology are shown. Dark and light gray indicate $\delta T = -0.1$ and $+0.1$, respectively. White spheres indicate the bottom of the mantle.

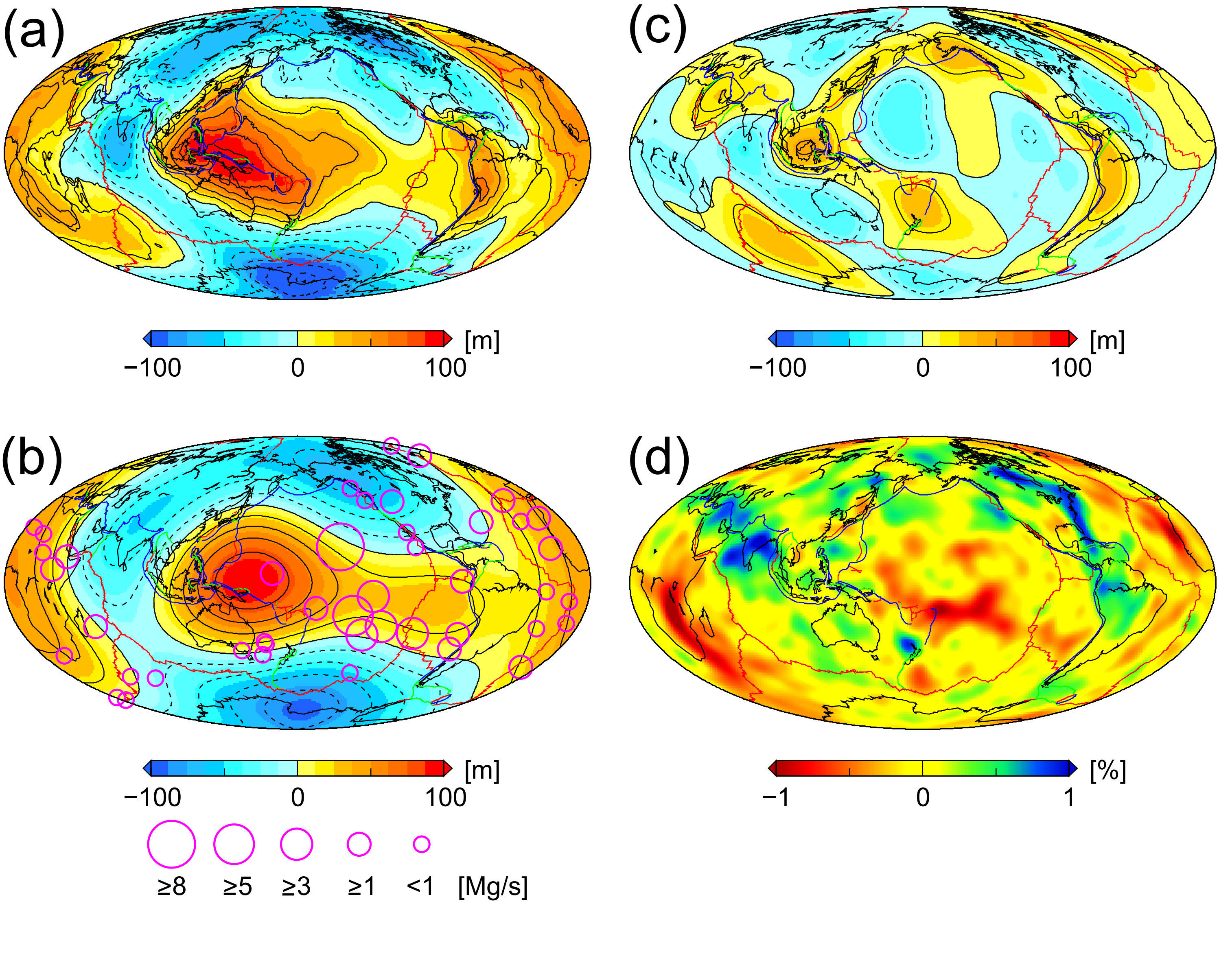

Fig.1 (Yoshida & Nakakuki)

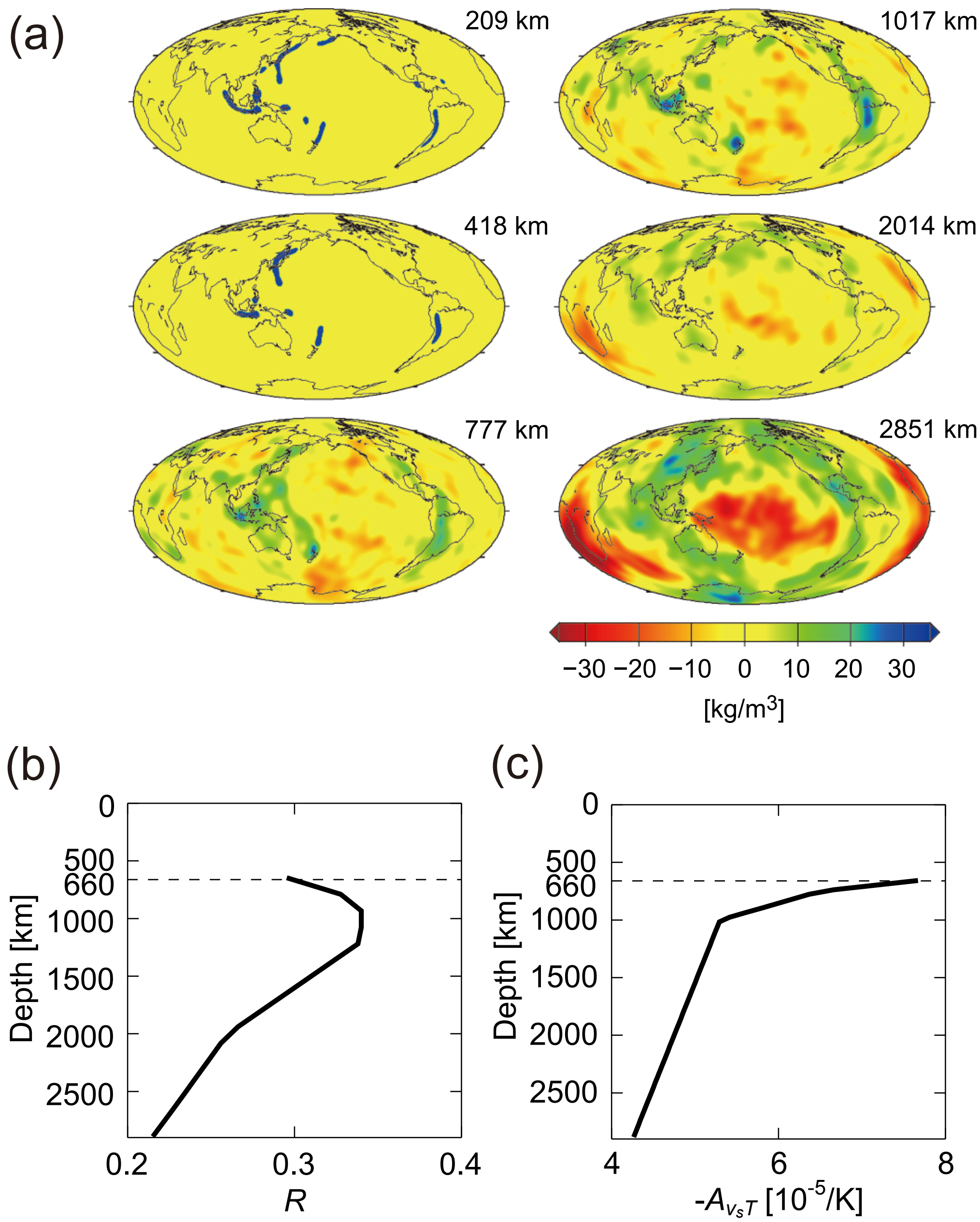

Fig.2 (Yoshida & Nakakuki)

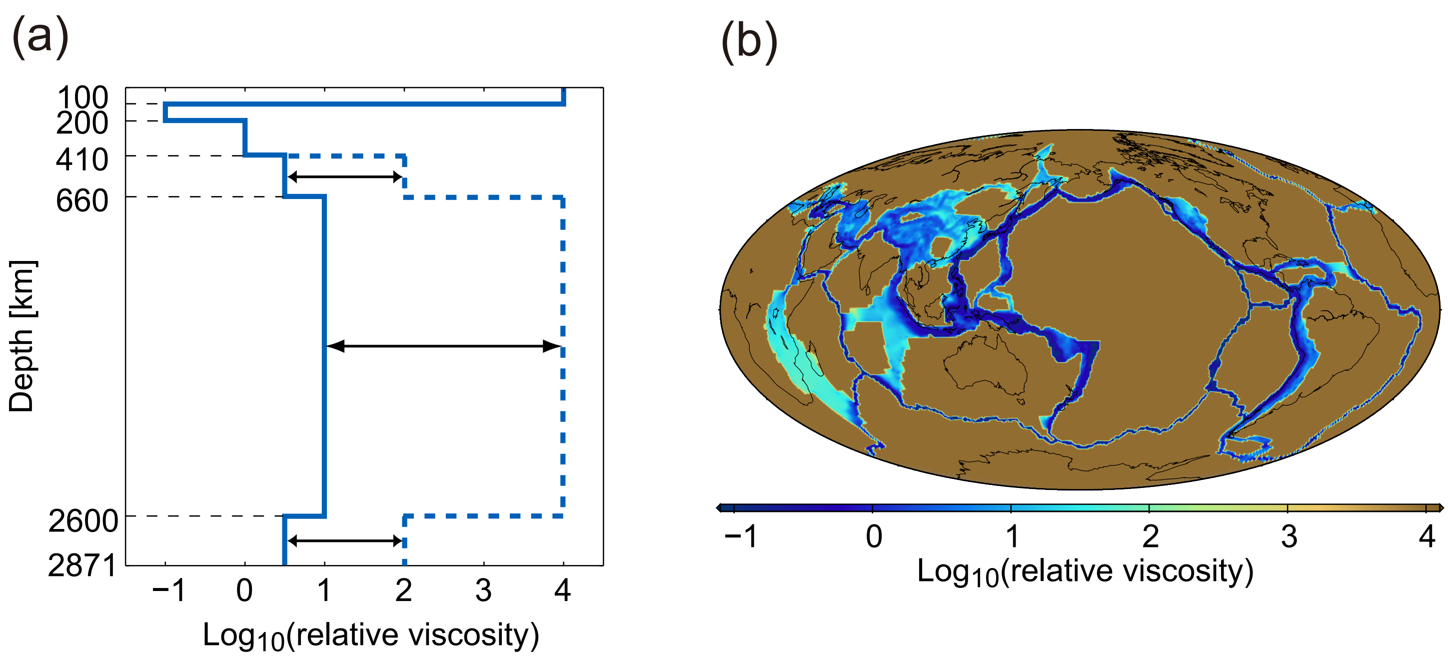

Fig.3 (Yoshida & Nakakuki)

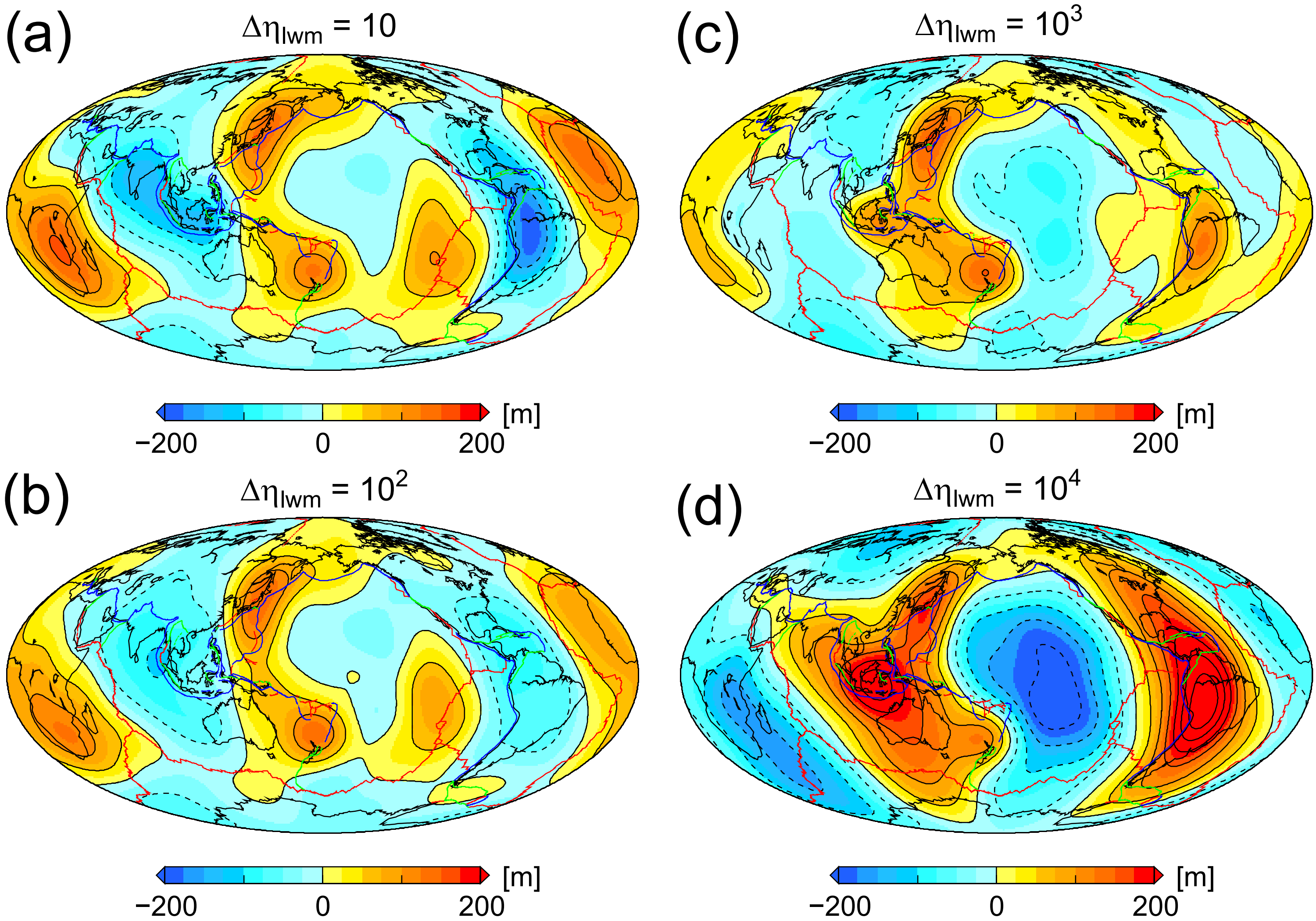

Fig.4 (Yoshida & Nakakuki)

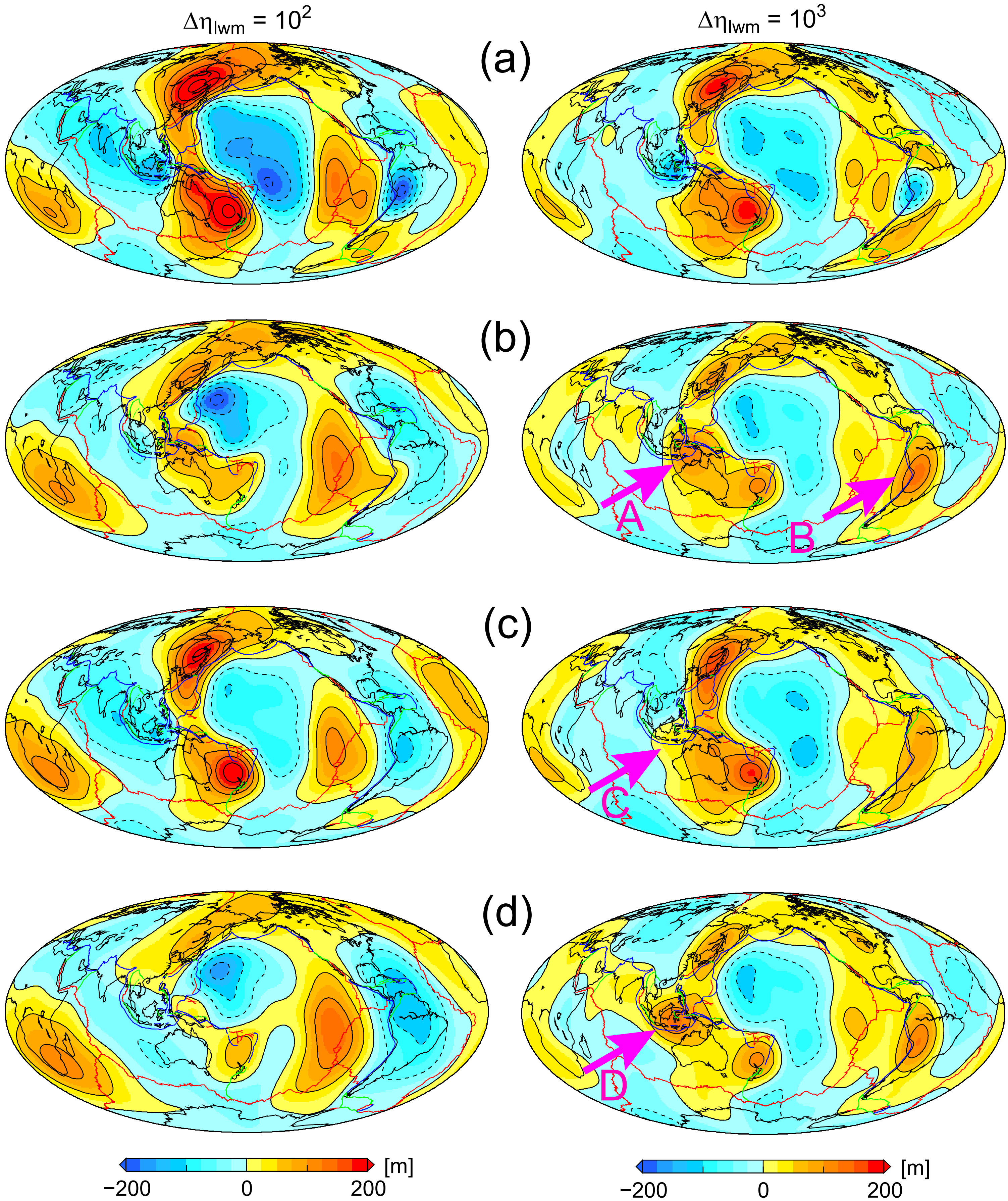

Fig.5 (Yoshida & Nakakuki)

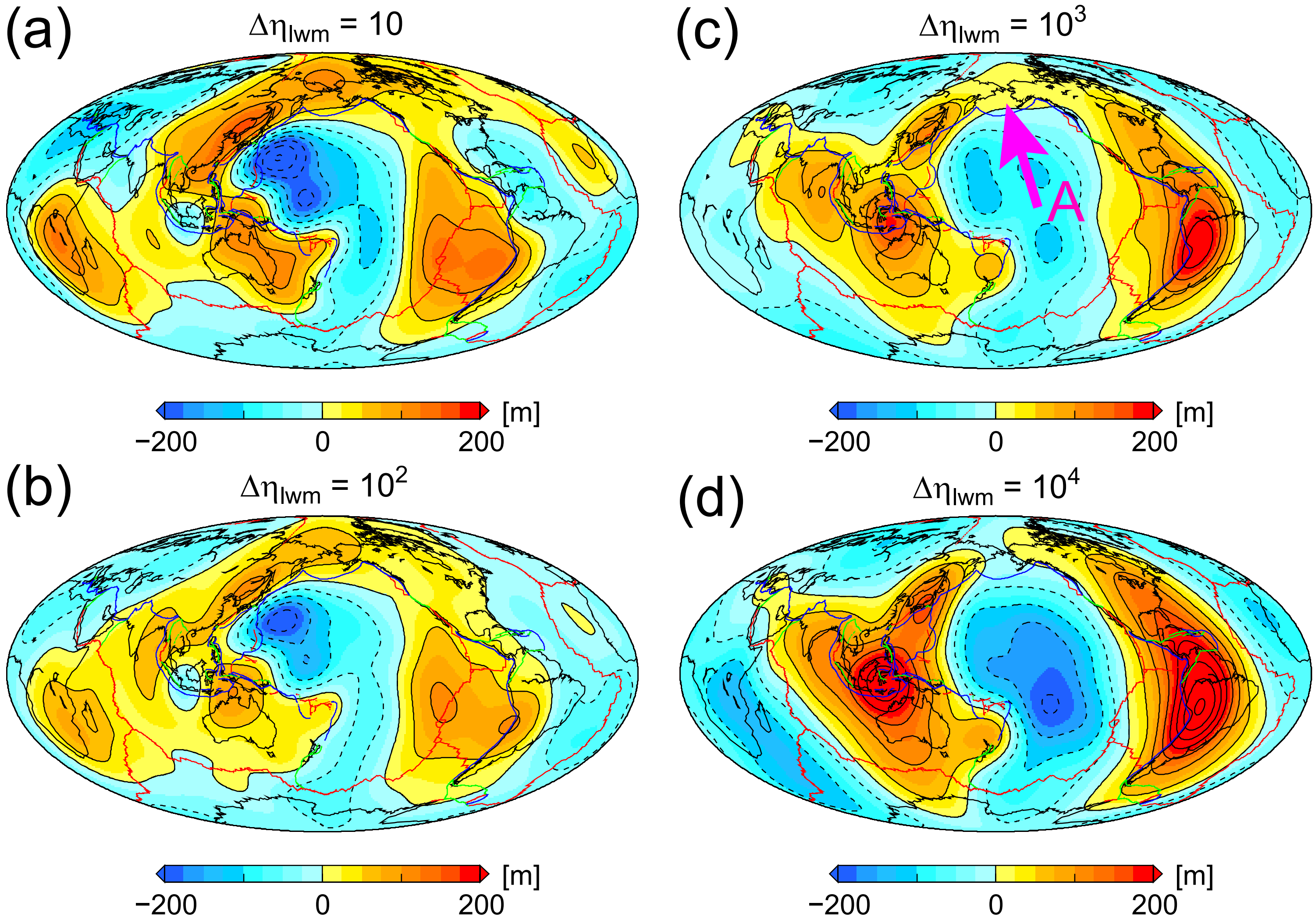

Fig.6 (Yoshida & Nakakuki)

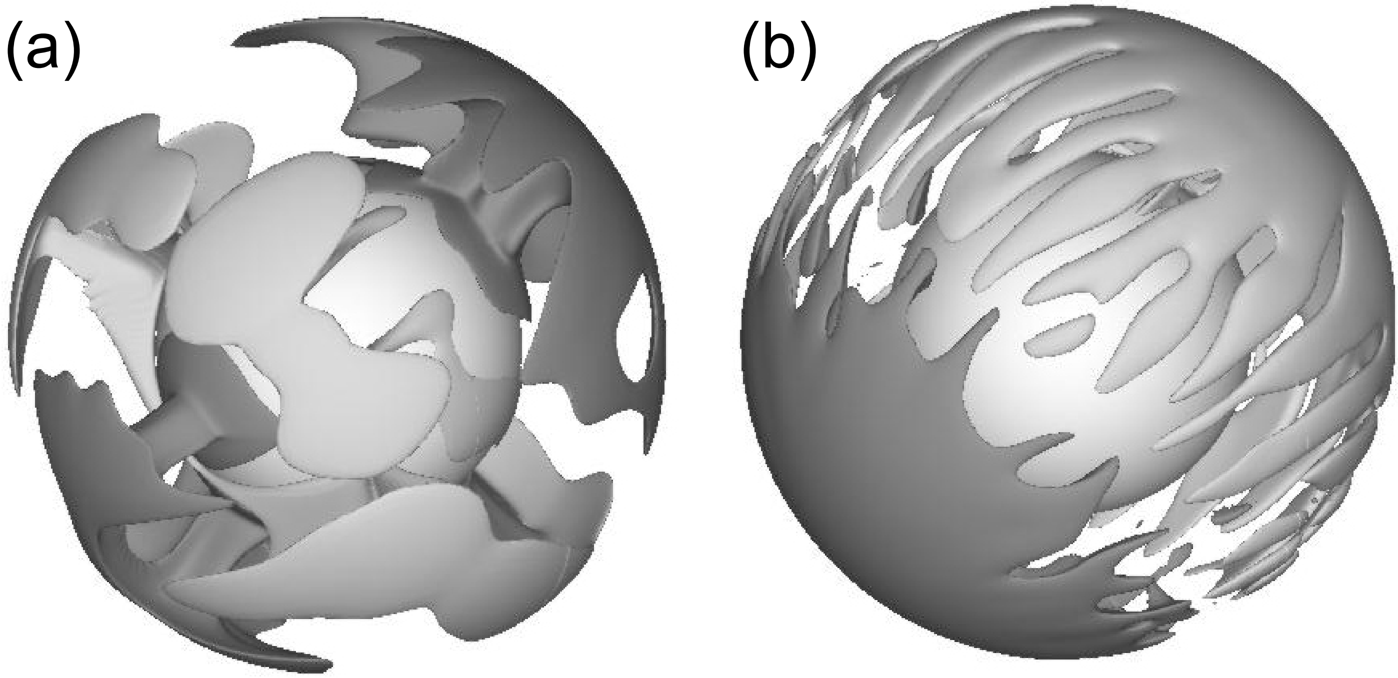

Fig.A.1 (Yoshida & Nakakuki)